ARTICLE OPEN

Check for updates

Investigating molybdenum's sulphur scavenging ability for MoS$_2$ formation in preventing pitting corrosion of stainless steels

Kai Xiang Kuah[1] and Daniel J. Blackwood [ID][1] ✉

The addition of Mo enhances pitting corrosion resistance in 304L stainless steel. However, there is no consensus on the underlying mechanism. One possible explanation is that molybdenum converts sulfide to stable MoS$_2$. This study investigates the effect of MoS$_2$ inclusion on the corrosion of 304L stainless steel by introducing both MnS and MoS$_2$ using spark plasma sintering. The reduction of MoS$_2$ to Mo is observed during the sintering process, contradicting the assumption that the sulfide inclusions can be stabilised by forming MoS$_2$. Therefore, MoS$_2$ formation cannot explain the improved corrosion resistance of 304L stainless steel with the addition of Mo.

INTRODUCTION

Steels as one of the most common forms of iron alloys, are important to our global economy and the advancement of our society. The world has witnessed a 120% increase in crude steel production over the past decade from 2000 to 2019, with China alone contributing 85% of the overall increase in production[1]. However, impurities in the steel can pose serious challenges during the application phase, the presence of sulfur (S) in particular is known to result in hot shortness of steel (through the formation of iron(II) sulfide (FeS)[2,3]) and is also detrimental to corrosion properties[4]. Fortunately, the majority of the sulfur inherent in the ores can be removed during the blast furnace process. Under ideal conditions, the S content in the final product can be lowered to a concentration of less than 0.001% (10 ppm), through a combination of hot metal pretreatment and secondary metallurgy treatments[5]. In the subsequent alloying phase, researchers have also recognized the benefit of manganese (Mn) additions to steel. The presence of Mn is known to suppress the precipitation and formation of FeS, improving the mechanical properties of steels[6]. The suppression of FeS formation by Mn can be viewed as a redox based reaction (Reaction 1), with the Fe^{2+} in FeS being reduced to Fe and the Mn being oxidized to Mn^{2+} forming manganese sulfide (MnS)[7,8].

$$Mn + FeS \rightarrow MnS + Fe \tag{1}$$

However, MnS precipitates are known to detrimentally influence the corrosion properties through an increased susceptibility of pit formation in both carbon steels[9] and stainless steels[10,11]. Although it is known that pitting corrosion is usually associated with MnS inclusions within the matrix[9–11], the removal of Mn and S from the alloy is not an option as both elements are required to provide desirable mechanical properties in the stainless steel[6,7]. One way to improve stainless steel's resistance to localized corrosion is the addition of molybdenum (Mo).

The addition of Mo improves both the anodic dissolution rate[12] and pitting resistance[13] of Fe–Cr alloys, easing the detrimental influence on the corrosion properties brought along by the presence of MnS inclusions[10,11]. From a comparison of the Nyquist plot of 304L (Mo-free) and the 316L (2 wt% Mo) obtained from electrochemical impedance spectroscopy by Polo et al.[14] in NaCl and Pardo et al.[15] in H$_2$SO$_4$ it can be seen that the presence of Mo has significantly improved the charge transfer resistance of the passive film. Likewise, detailed XPS studies of the passive film formed on the 316L stainless steel by Lynch et al.[16] attributed the improvement of the corrosion performance to the enrichment of the surface film by Mo. Alternatively, from a point defect model (PDM) point of view, the enrichment of Mo within the passive film results in a reduced number of point defects[17]. The thermodynamic properties of molybdenum, specifically its chemical activity, have also gained significant attention in the manufacturing industry. This is due to its remarkable ability to influence oxidation reactions, which in turn directly impacts the composition of the final steel[18].

However, despite decades of research into Mo stabilizing the passive film on Fe–Cr-based alloys[12,13,19–21], there are still differing opinions on the exact role that Mo plays in improved corrosion resistance. The predominant belief among researchers is that Mo improves the pitting resistance of stainless steels by enhancing the passive film and/or inhibiting dissolution kinetics. However, the nature of the passive film enhancement is ill-defined but is usually thought to be related to the formation and incorporation of Mo(IV) or Mo(VI) species in the surface passive film[16,19]. Clayton et al.[19] proposed that the incorporation and synergy between the molybdate (MoO$_4^{2-}$) and chromate (CrO$_4^{2-}$) in the passive film altered the ion selectivity from anion to cation, providing the necessary protection of the surface against aggressive attacks by hydroxide (OH$^-$) and chloride (Cl$^-$) ions. However, it is vague how the Mo(IV) or Mo(VI) species could interact with the MnS inclusions that are known to be the pit initiation sites. Notably, the pitting resistance can be significantly improved by reducing the size or eliminating MnS inclusions, as observed in 3D-printed 316L or the vacuum-melted 316LVM grade, even without altering the Mo content. While the point defect model (PDM) suggests that the presence of Mo(VI) in the passive film could impede defect migration and prevent pitting, this theory is not widely accepted within the corrosion community, due to inconsistencies with

[1]Department of Materials Science & Engineering, National University of Singapore, 9 Engineering Drive 1, 117575 Singapore, Singapore. ✉email: msedjb@nus.edu.sg

experimental observations[22,23]. Similarly, Mo in the stainless steel matrix can reduce the dissolution rate in the active pit, thereby lowering the rate at which the occluded pit solution becomes acidic via the hydrolysis of metallic ions and increasing the chances of repassivation occurring likely involving the repassivation of the active sites as the released molybdate ions for a protective layer of insoluble $FeMoO_4$[24]. However, it raises the question of whether a Mo content of 2 wt% (~1 at.%) is sufficient to significantly reduce the dissolution rate and tip the balance between repassivation and pit propagation. Jin et al. discovered that adding just 1 at.% (~1.7 wt%) of Mo to iron resulted in only a 10% decrease in the experimental dissolution rate in 1 M HCl[25].

Furthermore, there are other proposed mechanisms for how Mo improves pitting resistance, which include:

(a) Stabilizing the MnS sulfide inclusions by converting these to MoS_2 or $(Mo_xMn_y)S$ inclusions[26]. Several works have demonstrated the dissolution of MnS inclusions, which is one possible mechanism for pit initiation[27,28]. The chemical stability of MoS_2 is well-known, being able to maintain passivity across a wide pH range[29]. The stability of MoS_2 combined with its insolubility means that it will not be able to partake in dissolution during corrosion. Indeed, Ng et al.[30] determined that Mo alloying will thermodynamically improve the stability of the surfaces of MnS inclusions, reducing their dissolution tendency in the presence of chloride. However, this has yet to be supported by experimental data.

(b) It has been argued that the mechanism of the addition of molybdate inhibitor (MoO_4^{2-}) is similar to the presence of Mo as an alloying element for the improvement of pitting corrosion resistance of Fe–Cr alloy[31]. Following this train of thought, it may not be far-fetched to expect that a protective cap can be formed over the MnS inclusion[26], perhaps via the reaction of molybdate ions with sulfide or polysulphide ions to form a fine layer of MoS_2. However, it is unclear if the 2 wt% Mo (slightly more than 1 at.%) concentration used in 316L would be sufficient for such a mechanism to occur.

(c) Mo prevents chromium depletion, which is known to occur in the matrix/inclusion boundary region around the MnS inclusions[32]. However, in situ TEM studies by Kovalov et al.[27] found no evidence for $MnCr_2O_4$ nanocrystals that had previously been proposed as initiation sites for MnS dissolution and for causing the Cr depletion, so this last mechanism can likely be discounted.

In previous studies by Nishimoto et al.[33], the process of Cr enrichment of sulfide inclusions was positively correlated to the retardation in the sulfide inclusions' dissolution rate, improving the corrosion performance of Fe–Cr alloys. This raises the question —to what extent will the alloying elements interact with the sulfide inclusions and influence their dissolution kinetics? Based on the ab initio modelling conducted by Ng et al.[30], it was found that the presence of Mo can enhance the stability of the MnS surface in the presence of Cl^-. Not only does this indicate that incorporating Mo into the alloy has the potential to effectively counteract the degradation process, offering a promising avenue for enhancing the corrosion resistance of ferrous alloys, but also aligns with Mo's well-established inhibitory role during pitting corrosion[34]. However, there have been reports that Mo additions do not change the composition of existing MnS inclusions[34], as such the mechanism of Mo stabilising sulfide dissolution is not widely accepted within the corrosion community. This led us to the objective of this study, which is to clarify the potential interaction(s) of Mo with the S impurities in 304L stainless steel during the manufacturing process, in particular the possibility of the conversion of the unstable MnS inclusions into stable, insoluble MoS_2 or $(Mo_xMn_y)S$ inclusions.

This work starts with the spark plasma sintering of 304L stainless steel samples with and without minute additions (0.02 wt % by sulfur) of MnS or MoS_2 in the initial 304L stainless steel powder feedstocks. The initial powder feedstock and the sintered samples were then characterized with SEM, EDX and XRD. The post corrosion morphology of the inclusions within the 304L stainless steel samples was also reported and discussed. Finally, together with the experimental results and the help of thermodynamic calculations, the possibility of Mo interaction with the S impurities during the casting phase is discussed and concluded.

RESULTS AND DISCUSSION

Powder feedstock characterisation

Figure 1 shows the general morphology of the as received 304L powder, prepared 304L-MnS powder feedstock and prepared 304L-MoS_2 powder feedstock. The particles in the as-received 304L powder feedstock (Fig. 1a) were generally spherical in shape and uniform in radius, with a few irregular particles. After MnS and MoS_2 particles were, respectively, added to the as-received 304L powder and thoroughly mixed through mechanical tumbling (Fig. 1b, c), the powder feedstocks revealed neither agglomeration nor inhomogeneity.

Figure 2 shows the morphology of the 304L-MnS powder feedstock at high magnification, together with the elemental mapping of the same region with EDX. The elemental mapping shows particles rich in Mn and S among the added 304L powder. This confirms the presence of the added MnS. Figure 3 shows the morphology of the 304L-MoS_2 powder feedstock at high magnification, together with the elemental mapping of the same region with EDX. Strong intensity of Mo and S were observed in the secondary phases present among the 304L-MoS_2 powder; not out of the ordinary as MoS_2 particles were added. Although a lack of Mn signal in the added MoS_2 particle is expected, the contrast in the Mn signal will be back in the spotlight during the latter discussions of this work.

Characterisation of sintered samples

Figure 4 shows the XRD patterns of the as-received 304L powder, sintered 304L, sintered 304L-MnS and sintered 304L-MoS_2 samples. The XRD patterns reveal that the major constituent of all the samples was austenite (γ), with some martensite (α') phases. The presence of the austenite and martensite phases with their
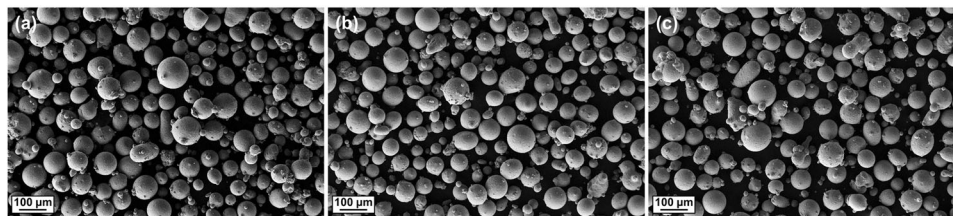

Fig. 1   SEM characterisation of the powder feedstock. a as received 304 L powder, **b** prepared 304L-MnS powder feedstock and **c** prepared 304L-MoS_2 powder feedstock.
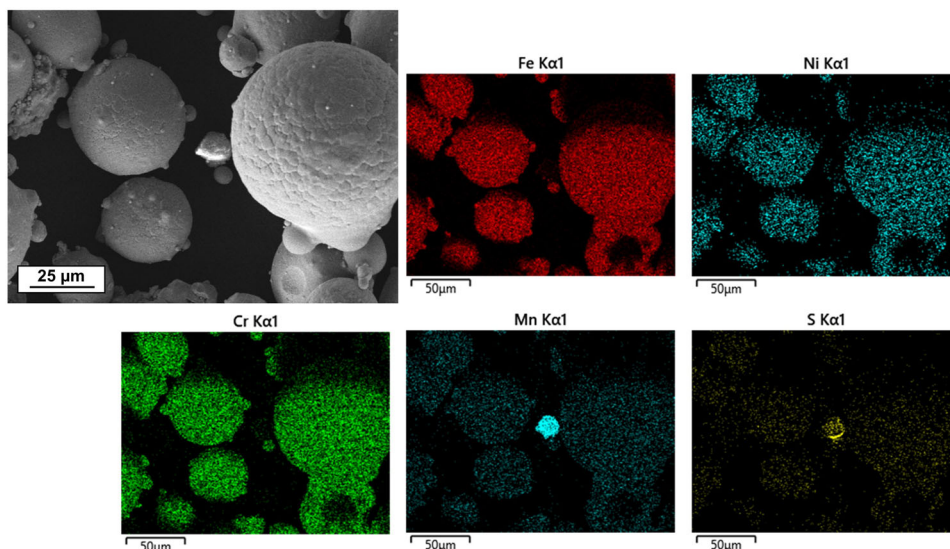
Fig. 2 SEM and EDX characterisation of prepared 304L-MnS powder feedstock. SEM and EDX identification of MnS in the prepared 304L-MnS powder feedstock.
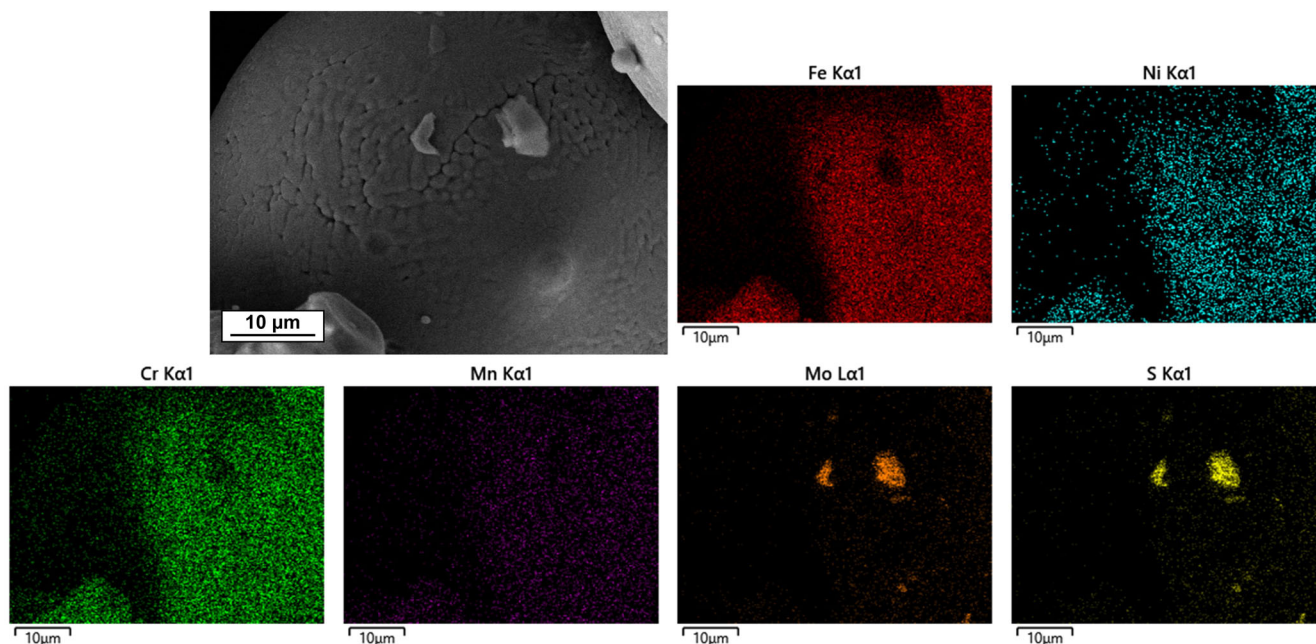

Fig. 3 SEM and EDX characterisation of prepared 304L-MoS$_2$ powder feedstock. SEM and EDX identification of MoS$_2$ in the prepared 304L-MoS$_2$ powder feedstock.

peak locations was as expected to be found in a 304L stainless steel material[35], the high austenitic percentage of the sintered samples attributed to the combination of Cr and Ni composition within the alloy[36]. It is not surprising that no peaks were observed from sulfur-rich phases in the XRD patterns 304L-MnS and sintered 304L-MoS$_2$ samples since the added amounts of sulfur (0.02 wt% S by mass) are well below the sensitivity and detection limit of the XRD machine (~1 vol%). The close similarity of the XRD pattern of the as received 304L powder with the rest of the sintered samples is indicative that no significant phase changes occurred during the spark plasma sintering process. After spark plasma sintering, the samples were left to cool naturally. As such the microstructural formation process was not controlled. Nonetheless, the XRD pattern of the sintered samples was observed to be uniform, allowing for a comparative study.

Figure 5 shows an SEM image along with EDX mapping of a sample's surface prepared from the sintering of the 304L powder. The surface morphology of the post sintered 304L revealed no significant presence of pores. The determined parameters for the spark plasma sintering were thus deemed to be sufficient in providing significant densification of the 304L powders. From the EDX mapping image, the elemental distribution is also observed to be uniform across the sintered sample surface. The element quantification by EDX (Table 1) revealed a surface composition (wt%) of 69.1% Fe, 19.9% Cr, 9.5% Ni and 1.5% Mn, which is in close agreement with the composition of the as received powder, indicating that there was no major compositional change caused by the spark plasma sintering of the 30L stainless steel. Similarly, from the composition of sintered 304L-MnS and sintered 304L-MoS$_2$ (Table 1), it can be concluded that no major compositional

change was caused by the addition of MnS and MoS$_2$ secondary phases to the powder feedstock used for spark plasma sintering of the stainless steel powder.

Although, based on the Fe–S phase diagram, it has been reported that the solubility of sulfur in the ferrite (α) phase is 0.01 wt%, while the solubility of sulfur in austenite (γ) is 0.05 wt%[37], the poor stability of any iron(II) sulfide (FeS) precipitated in the presence of Mn means that any FeS in the sintered 304 L samples will be reduced to Fe, accompanied by the oxidation of Mn to manganese (II) sulfide (MnS). The work of Lu et al.[8], demonstrated the preferential formation of MnS over FeS at elevated temperatures. Nonetheless, a lack of observation of any distinct precipitation of the above-mentioned sulfide-rich phases in the SEM images of sintered 304L can be attributed to the inherently low sulfur content of the as-received powder feedstock (40 ppm).

Figure 6a shows an SEM image of the general morphology of the sintered 304L-MnS along with a magnified micrograph showing the presence of inclusions, together with its EDX mapping. Similar to the sintered 304L, the sintered 304L-MnS also demonstrated significant densification after the spark plasma sintering. Unlike the 304L powder with low initial S content of 40 ppm, the initial addition of MnS particles (additional of 0.02 wt% sulfur) into the 304L-MnS powder feedstock significantly increases its S content
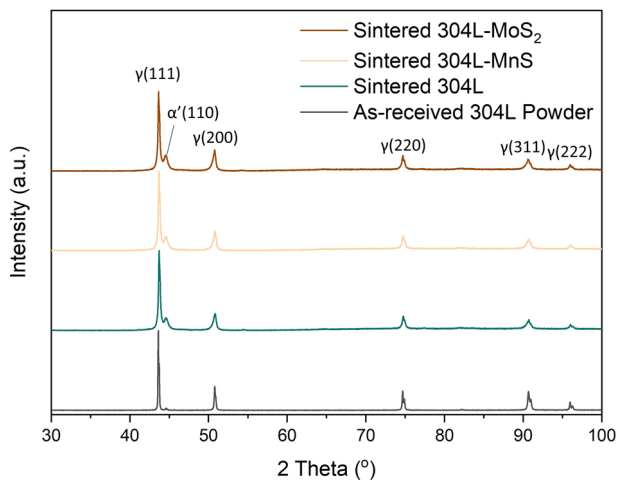
beyond its solubility limit, allowing the observation of sulfur-rich secondary phases, i.e. MnS inclusions.

Figure 6b shows an SEM image of the general morphology of the sintered 304L-MoS$_2$ along with a magnified micrograph showing the presence of inclusions, together with its EDX mapping. Similar to the case of sintered 304L and sintered 304L-MnS samples, the sintered 304L-MoS$_2$ sample also demonstrated significant densification post spark plasma sintering. Surprisingly, the elemental mapping of the sintered 304L-MoS$_2$ sample revealed the presence of Mn at the location of the sulfur secondary phase inclusion, which is in contrast to the pre-sintered sample where the absence of Mn in the MoS$_2$ particles was confirmed (Fig. 3). The enrichment in Mn was observed for all the sulfide inclusions on the surface of the sintered 304L-MoS$_2$.

Figure 7 shows the elemental composition (determined by EDX) of sulfur-rich inclusions found in the (a) mixed 304L-MoS$_2$ powder feedstock and its subsequent (b) sintered 304L-MoS$_2$. Here, values are reported in atomic percent (at.%), as opposed to wt% in the rest of the manuscript, for ease of structural identification. The ratio (at.%) of Mo:S and Mn:S of the sulfur-rich inclusion in the 304L-MoS$_2$ powder feedstock is found to be 1:1.8 and 1:94.8, respectively (Fig. 7a). The approximately 1:2 ratio of Mo:S confirms the identity of the sulfur-rich particle to be MoS$_2$, while the presence of trace manganese can be attributed to the excess penetration depth of the instrument, similar to the detection of iron, chromium and nickel. Post sintering, although the Mo signal still exist in the mapping, this is not reliable and can likely be attributed to a very close overlap of Sulfur Kα (2.307 eV) and Molybdenum Lα (2.293 eV). As such, the point analysis in Fig. 7 should be used for Mo confirmation. From Fig. 7b, deviation in the ratio (at.%) of Mo:S and Mn:S in the sulfur-rich inclusion in the sintered 304L-MoS$_2$ can be observed (Fig. 7b). The ratio (at.%) of Mo:S decreased to 1:30.8 (from 1:1.8), while the ratio (at.%) of Mn:S increased to 1:0.9 (from 1:94.8). The approximately 1:1 ratio of Mn:S post sintering indicates the presence of MnS. Although due to the excess penetration depth of the instrument, the exact composition of sulfur-rich inclusion cannot be precisely determined, the shift in the ratios of both Mo:S and Mn:S post sintering and the composition of Mo at a level <1 at.%, is clear evidence of the transformation of MoS$_2$ to MnS.

Figure 8 provides a schematic summary of the characterisation of the powder feedstocks and sintered samples. The spark plasma sintering of as received 304L powder resulted in a relatively dense sintered sample with no observed inclusion of sulfur-rich phase. This is as expected given the low sulfur content (40 ppm) of the as-received 304L powder as previously discussed. With the addition of MnS particles into the as received 304L powder feedstock, the sintering of the 304L-MnS powder feedstock

Fig. 4 XRD pattern of powder feedstock and sintered samples. XRD pattern of the 304L powder feedstock and spark plasma sintered 304L, sintered 304L-MnS and sintered 304L-MoS$_2$ samples.
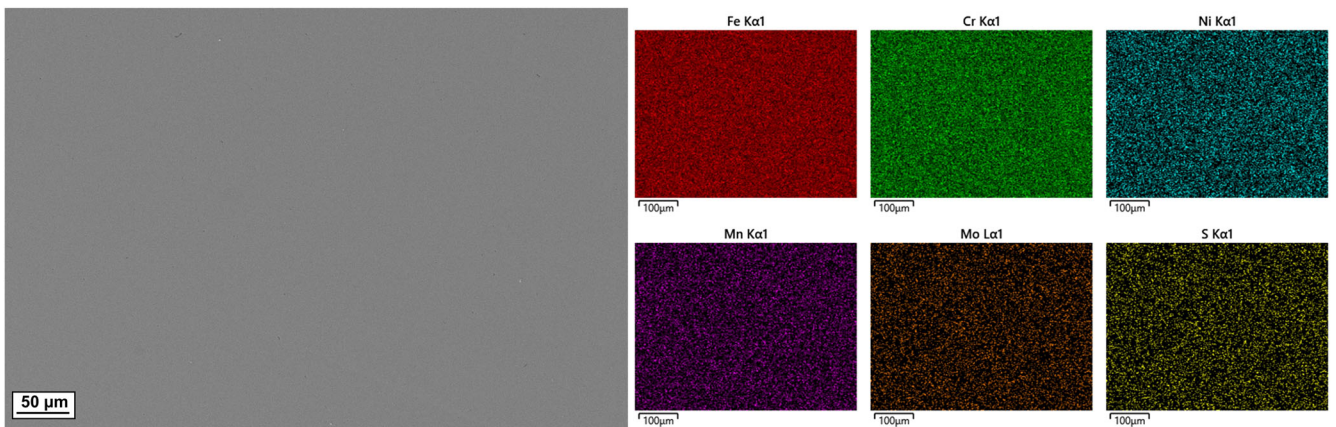

Fig. 5 SEM and EDX characterisation of sintered 304L. SEM and EDX characterisation of sintered 304L, showing the sample's general surface morphology and elemental distribution.

resulted in the inclusion of Mn-rich sulfur phases within the 304L stainless steel matrix of the sintered sample. However, the characterisation of the inclusions within the sintered 304L-MoS$_2$ did not reveal the presence of MoS$_2$, but instead, inclusions of Mn-rich sulfur were observed. This means that the addition of MoS$_2$ into the as received 304L powder feedstock resulted in the formation of Mn-rich S phases within the 304L stainless steel matrix of the sintered sample.

Thermodynamic interactions between alloying elements and sulfur

As previously mentioned in the introduction, inherent sulfur contamination during the iron ore processing results in the formation of FeS. The presence of these FeS within the micro-structure of the final cast product is known to lower the mechanical properties; an increase in observed brittleness. Mn is therefore added to the steel to supress FeS formation via Reaction 1.

Table 1. Elemental composition of sintered samples.

Sample	Composition (wt%)					
	Fe	Cr	Ni	Mn	Mo	S
Sintered 304L	69.1	19.9	9.5	1.5	0	0
Sintered 304L-MnS	69.3	19.5	9.6	1.5	0	0.1
Sintered 304L-MoS$_2$	68.3	20.1	9.4	1.6	0.4	0.1

Elemental composition of the sintered 304L, sintered 304L-MnS and sintered 304L-MoS$_2$ samples after spark plasma sintering determined by EDX.

Nonetheless, this reaction will only be plausible if there exists a thermodynamically favourable interaction between the FeS and Mn.

Figure 9a shows the Gibbs free energy change of Reaction 1 between FeS and Mn, calculated from 600 to 2000 K; calculations were conducted based on per mole FeS participated in the reaction. The calculations also considered the most stable phases at each temperature, taking any potential change in phase (e.g. melting from solid to liquid) into consideration. The numerical results are tabulated in Table 2. Although a positive shift in the Gibbs free energy with temperature is observed, the overall calculated Gibbs free energy of the reaction is negative over the entire calculated temperature range, suggesting the spontaneity of the reaction between FeS and Mn. Therefore, since the temperature of conventional casting is in the range of ~1400 °C/1673 K, the reaction between Mn and FeS is expected to be spontaneous, which has been demonstrated experimentally[6,7]. This observation has also been attributed to the presence of Mn suppressing the formation of FeS in favour of MnS at an elevated temperature of 1843 K[8].

From the observed reduction of FeS in the presence of Mn during conventional casting, it is reasonable to draw parallels between the observation made during the sintering of 304L-MoS$_2$ with that of the conventional casting of stainless steel. Similar to conventional casting where the MnS is formed through the reduction of FeS to Fe in the presence of Mn (Reaction 1), Mn enrichment of the sulfur-rich secondary phase is observed in the post sintered 304L-MoS$_2$ (Fig. 6b). This sulfur-rich secondary phase was previously identified to be MoS$_2$ during the characterisation of the powder feedstock (Fig. 3). This observation suggests the enrichment of sulfur-rich secondary phase of the sintered 304L-MoS$_2$ sample by Mn, through the diffusion of Mn into MoS$_2$, forming MnS during the sintering process. Reduced Mo then can diffuse to the surrounding matrices based on the following
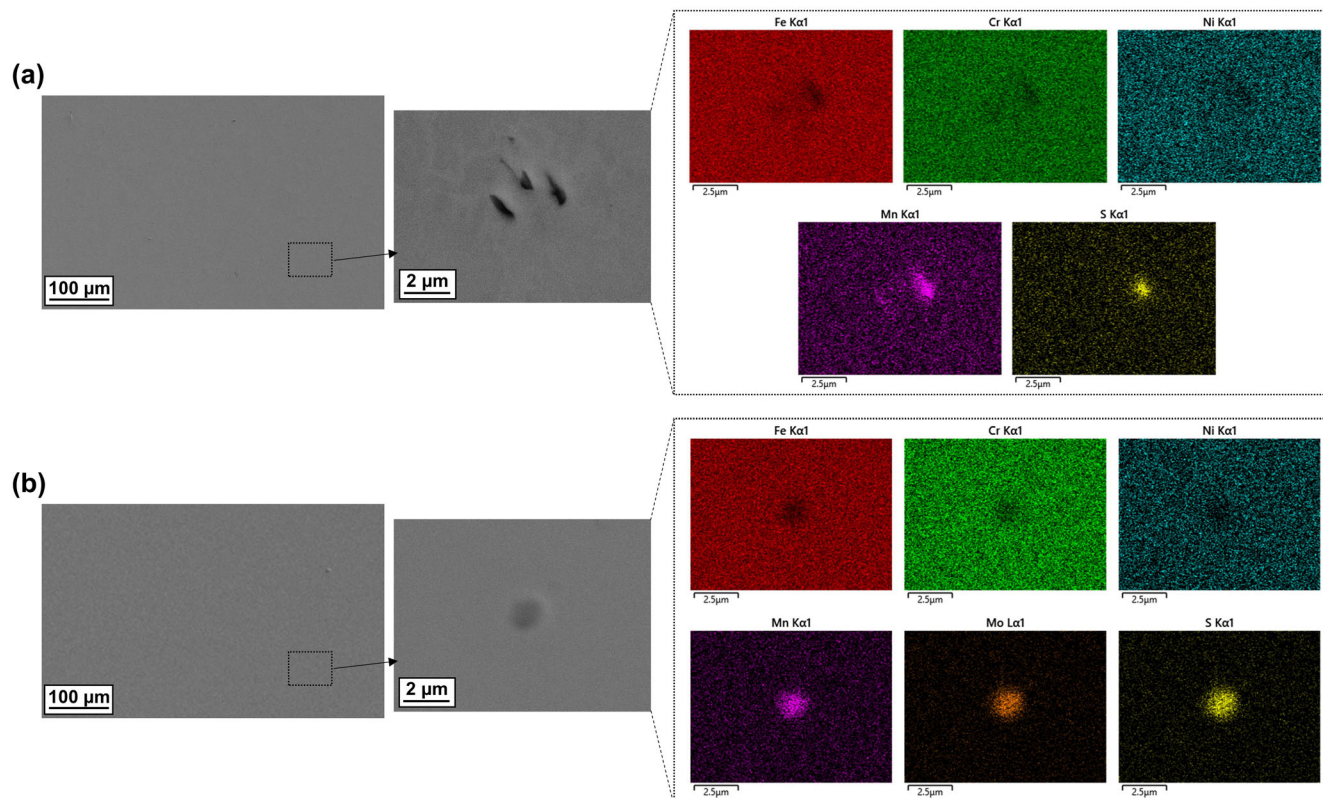

Fig. 6   SEM and EDX characterisation of sintered 304L-MnS and 304L-MoS$_2$ samples. SEM and EDX of **a** sintered 304L-MnS and **b** sintered 304L-MoS$_2$, showing the sample's general surface morphology and the identification of their respective sulfur-based inclusions.

equation:

$$2Mn + MoS_2 \rightarrow 2MnS + Mo \qquad (2)$$

However, any potential redox reaction of MoS_2 to MnS in the presence of Mn will require favourable thermodynamics, similar to the case of conventional casting where MnS is formed through the reduction of FeS to Fe (Reaction 1). To study the feasibility of the transformation of MoS_2 to MnS in the presence of Mn, thermodynamic calculations based on the above Reaction 2 were carried out.

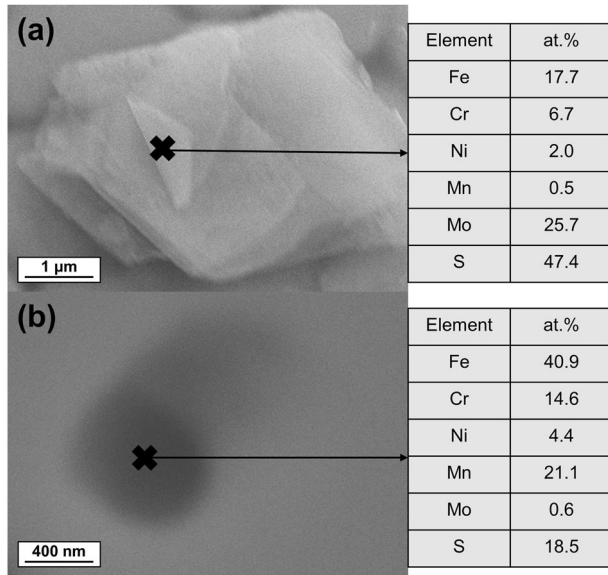Figure 9b shows the Gibbs free energy change of Reaction 2, determined from 600 to 2000 K; calculations were based on per mole MoS_2 participated in the reaction. Again, the calculations also considered the most stable phases at each temperature, taking any potential change in phase (e.g. melting from solid to liquid) into consideration. From 10b, it can be seen that the Gibbs free energy change of reaction becomes more negative when temperature increases from 600 K to approximately 1458 K, while the reactants are still in their respective solid states. It is possible to infer that the spark sintering temperature of 1273 K used in this work falls within the range of solid phase sintering of the added inclusions in the powder feedstock. The increased pressure applied during the spark plasma sintering will only serve to increase the melting temperature and extend the solid phase sintering window to a higher temperature. Nonetheless, at high temperatures of the spark plasma sintering, sufficient kinetics for the diffusion of the above-mentioned atomic species can be assumed, together with sufficient energy possessed by the individual species to overcome any potential energy barrier for the redox reaction. Note that although once the MoS_2 melts the Gibbs free energy change starts to increase slightly, the overall calculated Gibbs free energy of the reaction is negative over the entire calculated temperature range, suggesting that spontaneous reaction between MoS_2 and Mn will also occur in conventional casting.

The mechanistic transformation of MoS_2 to MnS during the sintering of 304L-MoS_2 powder feedstock can be summarized by the schematic presented in Fig. 10. Under a low kinetics situation, such as when the powder feedstocks were prepared at ambient temperature, the 304L powder and MoS_2 secondary phase do not react with each other. However, with the increase in kinetics during the high-temperature sintering, the favourable thermodynamic relationship for the reduction of MoS_2 by Mn (as determined in Fig. 9b) becomes kinetically feasible, the pre-existing MoS_2 in the 304L-MoS_2 powder feedstock is reduced to Mo in the presence of Mn during the spark plasma sintering process, forming MnS in the process. The Mn in the surrounding 304L matrix is expected to diffuse to the MoS_2 secondary phase in the presence of the high kinetics due to high sintering temperature, reducing the Mo^{4+} to Mo. The oxidized Mn^{2+} binds with the sulfur, forming MnS. The newly reduced Mo then diffuses to the nearby 304L matrixes. This redox process between the Mn and Mo is expected to be continuous during the sintering
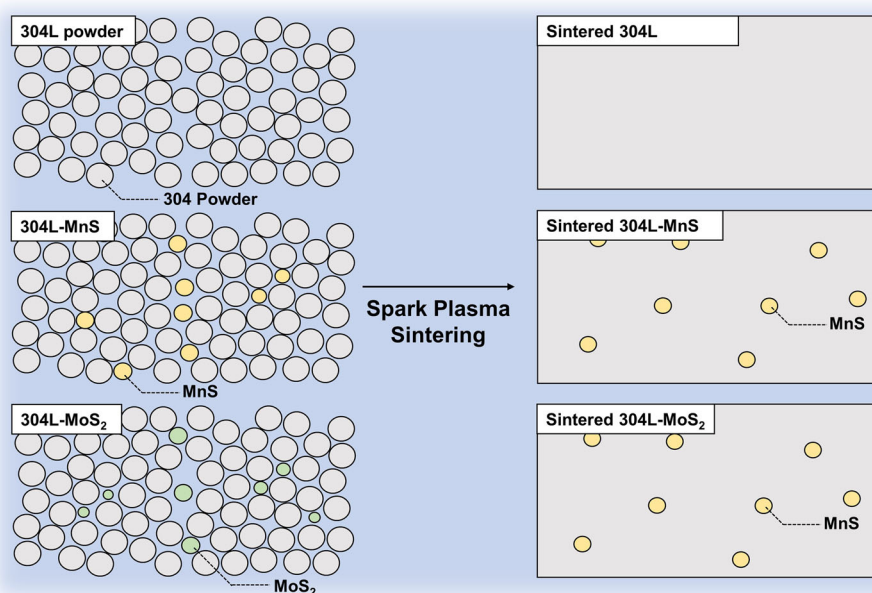

Element	at.%
Fe	17.7
Cr	6.7
Ni	2.0
Mn	0.5
Mo	25.7
S	47.4

Element	at.%
Fe	40.9
Cr	14.6
Ni	4.4
Mn	21.1
Mo	0.6
S	18.5

Fig. 7 Composition quantification of sulfur-rich inclusions in powder feedstock and sintered 304L-MoS_2 sample. Composition of the sulfur-rich inclusions in **a** 304L-MoS_2 powder and **b** sintered 304L-MoS_2.

Fig. 8 Morphology of powder feedstock pre and post sintering. Schematic showing the characterisation of the powder feedstock and sintered samples.
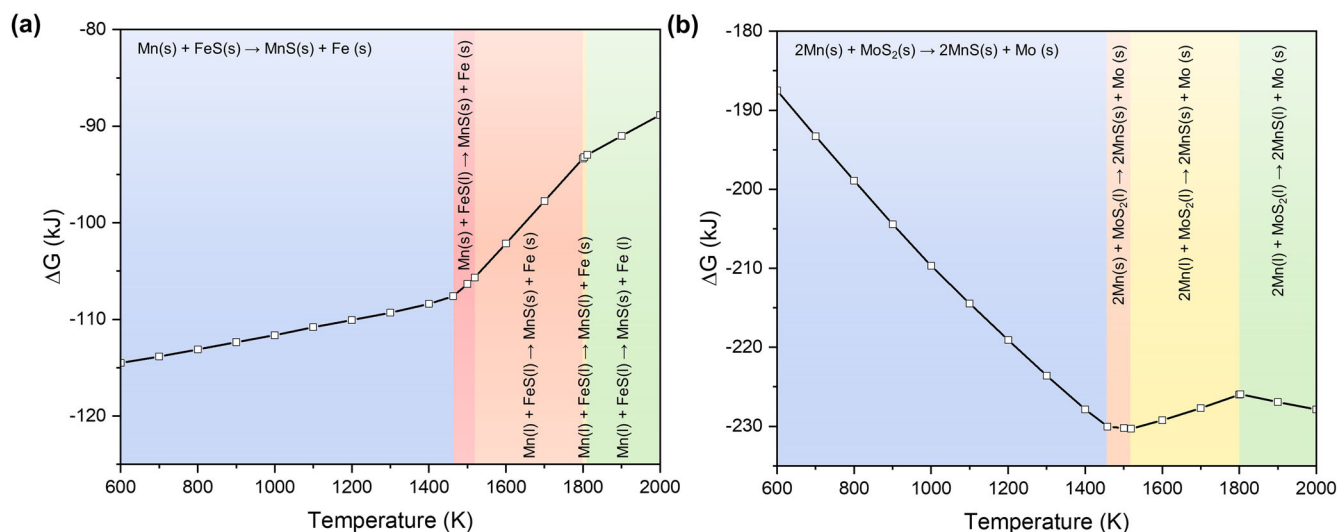
Fig. 9 Thermodynamic calculation of FeS and MoS₂ in presence of Mn. Gibbs free energy change of the reduction processes of **a** FeS and **b** MoS₂ by Mn with the temperature change. Thermodynamic calculations were conducted based on the equilibrium phases at the given temperature, taking into consideration any potential phase changes. The values of Gibbs free energy are reported based on per mole FeS and MoS₂ reduced, respectively.

Table 2. Thermodynamic calculations of reactions between FeS and MoS₂ with Mn.

Reactions of Mn with FeS			Reactions of Mn with MoS₂		
Reaction	T (K)	ΔG (kJ)	Reaction	T (K)	ΔG (kJ)
$Mn(s) + FeS(s) \rightarrow MnS(s) + Fe(s)$	600	−114.5	$2Mn(s) + MoS_2(s) \rightarrow 2MnS(s) + Mo(s)$	600	−187.5
	700	−113.8		700	−193.9
	800	−113.1		800	−198.9
	900	−112.4		900	−204.4
	1000	−111.6		1000	−209.7
	1100	−110.8		1100	−214.5
	1200	−110.7		1200	−219.1
	1300	−109.3		1300	−223.6
	1400	−108.6		1400	−227.9
$Mn(s) + FeS(l) \rightarrow MnS(s) + Fe(s)$	1463	−107.6	$2Mn(s) + MoS_2(l) \rightarrow 2MnS(s) + Mo(s)$	1458	−230.0
	1500	−106.3		1500	−230.2
$Mn(l) + FeS(l) \rightarrow MnS(s) + Fe(s)$	1519	−105.7	$2Mn(l) + MoS_2(l) \rightarrow 2MnS(s) + Mo(s)$	1519	−230.3
	1600	−102.1		1600	−229.2
	1700	−97.8		1700	−227.7
	1800	−93.3		1800	−226.0
$Mn(l) + FeS(l) \rightarrow MnS(l) + Fe(s)$	1803	−93.2	$2Mn(l) + MoS_2(l) \rightarrow 2MnS(l) + Mo(s)$	1803	−226.0
$Mn(l) + FeS(l) \rightarrow MnS(l) + Fe(l)$	1811	−93.0		1900	−226.9
	1900	−91.0		2000	−227.9
	2000	−88.8			

Gibbs free energy change for the reduction of (a) FeS and (b) MoS₂ by Mn over the temperature range 600 to 2000 K. Thermodynamic calculations were conducted based on the equilibrium phases at the given temperature, taking into consideration any potential phase changes. The values of Gibbs free energies are reported based on per mole FeS and MoS₂ reduced, respectively.

process, or until none of the MoS₂ remains. A similar result would also be expected if conventional casting had been used. In summary, the poor thermodynamic stability of MoS₂ in the presence of Mn at elevated temperatures explains the absence of MoS₂ from the sintered 304L-MoS₂ sample within the observation range of EDX (Fig. 7b).

Now that we have discussed the favourable thermodynamics for MoS₂ to form MnS in the presence of Mn, we may have to reconsider the potential presence of Mo in the sulfur-rich secondary phase as suggested by Ilevbare et al.[26]. As previously discussed in the introduction, MnS is detrimental to corrosion due to it becoming an anode when in contact with the surface film of stainless steel. This issue had been mostly averted with the addition of Mo during the conventional casting process, which has been demonstrated to improve the pitting/corrosion performance of stainless steels; admittedly the interactions between Mo and MnS
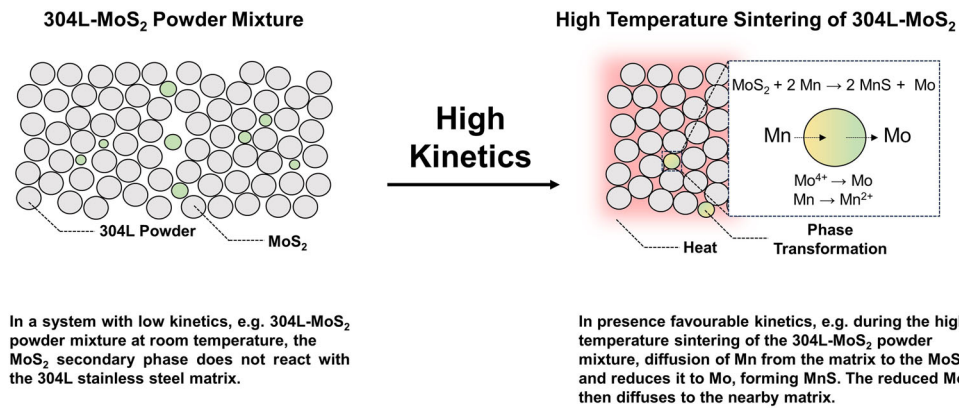
304L-MoS₂ Powder Mixture

High Temperature Sintering of 304L-MoS₂

Fig. 10 Reduction of MoS₂ by Mn during spark plasma sintering. Schematic explaining the mechanistic transformation of MoS₂ to MnS due to the thermodynamically favourable reduction of MoS₂ in the presence of Mn under high kinetics. The reduction of MoS₂ to Mo by Mn results in the formation MnS, with the reduced Mo diffusing to the surrounding matrix.
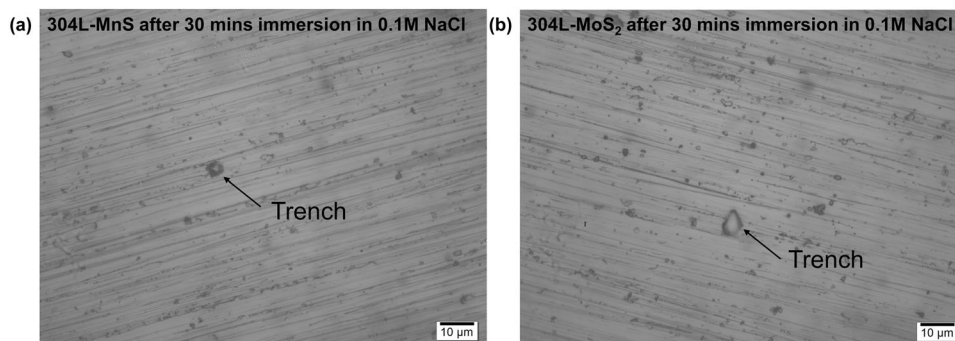

Fig. 11 Corrosion morphology of sintered samples during immersion corrosion. Optical image of **a** sintered 304L-MnS surface and **b** 304L-MoS₂ surface after 30 min immersion in 0.1 M NaCl. Arrows indicate the location of the trench on the respective sample surface.

inclusions remain unknown. From a thermodynamic standpoint, Fig. 9b shows that the addition of Mo during the casting process will not reduce the MnS to MoS₂ and Mn due to the significant thermodynamic barrier of the reverse reaction (Reaction 2), even at elevated temperatures. Similarly, the presence of Mn during the casting process will reduce any MoS₂ formed at any stage in the production process to MnS and Mo, due to the favourable thermodynamics and the presence of high kinetics (from the high casting temperature) to overcome potential reaction barriers; similar to the sintering of the 304L-MoS₂ powder feedstock presented in this work. This means that the formation of MoS₂ during the casting process of stainless steel containing both Mo and Mn as an alloying element cannot be expected; given that sulfur levels in stainless steel are <0.1 wt%. MoS₂ formation is still not expected even if the Mo percentage exceeds that of the Mn. The observation compliments the previous findings by Nishimoto et al.[34], where despite their adding of Mo to stainless steel, it was reported that 'there was little to no difference in the chemical composition of the inclusions in the Mo-free and Mo-added specimens', with the inclusions in the above quote referring to MnS.

Corrosion morphology

Although the composition characterisation and thermodynamic calculation highlighted the instability of MoS₂ in the presence of Mn, it is still worthwhile to support the results with the comparison between the corrosion morphology of the MnS that was phase transformed from MoS₂ (MnS in sintered 304L-MoS₂) with the MnS that did not undergo phase transformation (MnS in sintered 304L-MnS). Figure 11 shows the surface morphologies of the sintered 304L-MnS and 304L-MoS₂ samples after 30 min

immersion under open circuit conditions in 0.1 M NaCl, revealing the existence of a trench surrounding the MnS inclusion in both sintered 304L-MnS and in sintered 304L-MoS₂; as labelled in the respective optical images. The dissolution of MnS in 304L stainless steel after immersion in 0.1 M NaCl had been previously recorded[38], with the morphology of the trenches formed in this work resembling those described in the work of Yang et al.[39] and Nishimoto et al.[34]. The pitting susceptibility of 304L stainless steel is dependent on the presence of large (radius >0.5 μm) sulfide inclusions[40]. This subsequent dissolution of the sulfide inclusions severely reduces the pitting resistance of the stainless steel, leaving behind trenches and pits, and disrupting the passive film formed[41]. Nonetheless, it has also been proposed in the work of Rieders et al.[9], that it is not the dissolution of the MnS inclusions that causes pit initiation, but rather it is the presence of localised strain at the interfaces between the α-Fe and inclusions that are responsible for the formation of these trenches and pits. With the absence of inclusions nor trenching observed in sintered 304L after 30 min immersion under open circuit conditions in 0.1 M NaCl, it is therefore clear that the additional sulfur is detrimental to the pitting corrosion resistance of the sintered 304L stainless steel, regardless of whether it is added in the form of MnS or MoS₂.

While potentiodynamic polarisation tests can serve as an useful characterisation method for investigating the impact of MnS on the pitting resistance of 304L stainless steel, the presence of inherent micropores formed during the spark plasma sintering process despite the high pressure and temperature[42] can introduce complications during results interpretation. Similar to MnS, it is known that presence of inherent micropores have a detrimental effect on the corrosion performance of alloys[43,44]. This makes the process of distinguishing whether the observed current
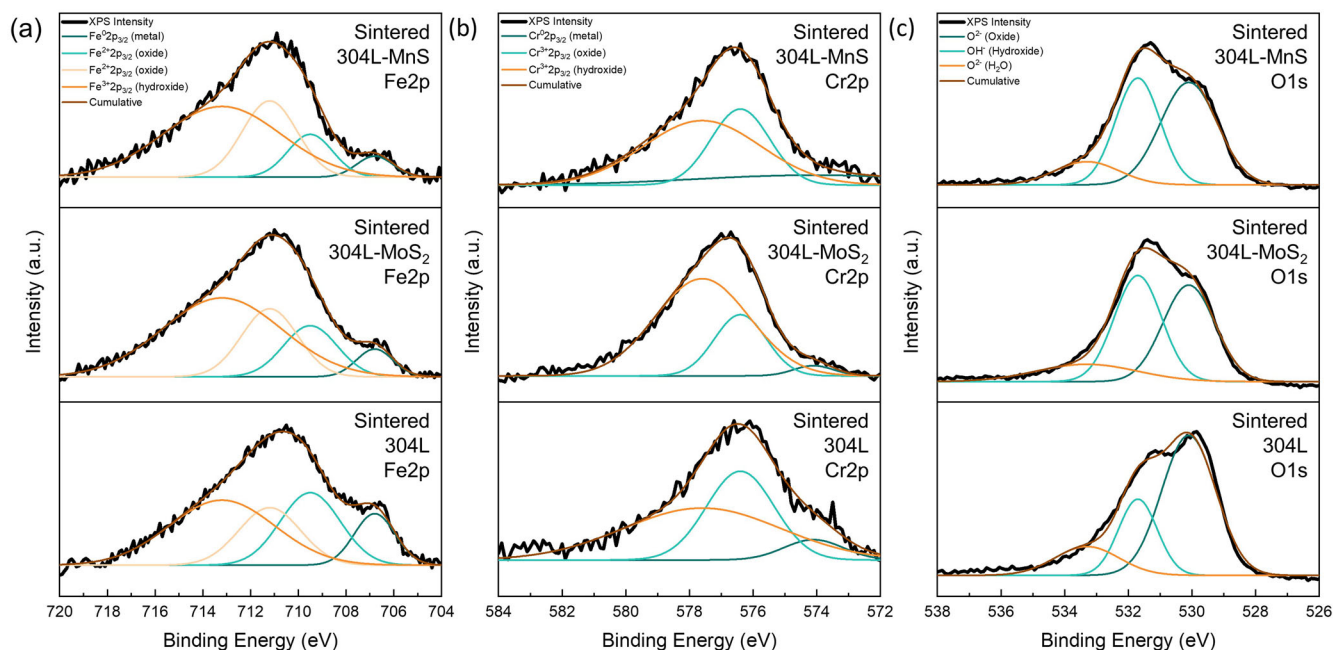
Fig. 12   XPS spectra from sintered sample surface post immersion. XPS spectra of **a** Fe2p, **b** Cr2p and **c** O1s of sintered 304 L, sintered 304L-MoS$_2$ and sintered 304L-MnS after 1-h immersion in 0.1 M NaCl.

response originates from the sulfide inclusion or from the inherent micropores challenging.

Figure 12 shows the XPS spectra of (a) Fe2p, (b) Cr2p and (c) O1s of sintered 304L, sintered 304L-MoS$_2$ and sintered 304L-MnS samples after 1-h immersion in 0.1 M NaCl. From the comparison of the Fe2p spectra, it is evident that there is an increase in the Fe^{3+} to Fe^{2+} ratio for the samples with added sulfide. Similarly, from the Cr2p and O1s spectra, an increase in hydroxide to oxide ratio was also observed for the samples with added sulfide. The increased Fe^{3+} to Fe^{2+} ratio at higher sulfide levels could be indicative of an increase in the thickness of the passive film, but thicker films are usually associated with improved passivity, so it is more likely that the increased Fe^{3+} is associated with the trenches seen on the sintered 304L-MoS$_2$ and sintered 304L-MnS samples[45]. Likewise, the increased OH$^-$ to O^{2-} ratio could be associated with an increasing thickness of the exchange outer layer of the surface oxide film[16] but is again more likely related to corrosion products that form during the trenching of MnS during immersion in 0.1 M NaCl (Fig. 11). Unfortunately, the resolution of the available XPS was unable to isolate the contributions of the surface film from the corrosion products formed in the trenches around the inclusions.

Although this work has been unable to identify the mechanism by which Mo improves the pitting resistance of 304L stainless steel, it has shown that one of the proposed mechanisms, stabilizing the sulfide inclusions, can be ruled out. The results obtained above clearly demonstrate that the proposition of stabilizing the MnS sulfide inclusions by converting these to MoS$_2$ or (Mo$_x$Mn$_y$)S inclusions[26] is flawed. The possibility of Mo scavenging for sulfur to form MoS$_2$ in the presence of Mn would require the overcoming of a significant thermodynamic barrier which is deemed unlikely. Under the high temperature during the manufacturing process in the presence of Mn, the formation of MoS$_2$ will be suppressed, similar to the example of the suppressed formation of FeS in the presence of Mn[8] due to the favourable thermodynamic formation of MnS under both scenarios. This thermodynamic relationship makes the formation of MoS$_2$ during both sintering and casting thermodynamically unfavourable and nullifies any possible benefits that an insoluble MoS$_2$ can potentially bring during corrosion as observed during the immersion corrosion of the sintered 304L-MoS$_2$ sample in 0.1 M NaCl.

This work used experimental validation and thermodynamic calculations to investigate the potential of Mo acting as a sulfide scavenger during the manufacturing process of 304L stainless steel, thereby stabilizing the MnS inclusions associated with pitting corrosion by converting these to MoS$_2$. Through the characterisation of inclusions and corrosion characteristics of spark plasma sintered MnS and MoS$_2$ containing 304L stainless steel powder, together with the thermodynamic calculations of the stability of MoS$_2$ in the presence of Mn the following verdicts can be reached:

1. During the characterisation of post sintered 304L-MoS$_2$ samples, it was found that instead of the MoS$_2$ that was initially added to the powder feedstock, the sulfide inclusions were in the form of MnS.
2. Thermodynamic calculations revealed that the reduction of Mo^{4+} to Mo in the presence of Mn is favourable at elevated temperatures, corresponding to the temperature range during both sintering and casting.
3. Increasing the sulfur content of 304L from ca. 0.004 wt% to 0.02 wt% resulted in the trenching of sulfide inclusion, regardless of whether the sulfur is added in the form of MnS$_2$ or MnS.
4. XPS measurements revealed that the addition of 0.02 wt% of S in the form of MoS$_2$ or MnS made no significant difference to the nature of the passive film.

METHODS

AISI 304L stainless steel powder and feedstock preparation

AISI 304L Stainless steel powder was supplied from Goodfellow Cambridge Limited with the supplier providing stating that the measured composition of 18.62 wt% Cr–9.52 wt% Ni–1.3 wt% Mn and balance Fe. The powder was also reported by the supplier to have a particle size distribution of Dv$_{10}$ = 54.3 μm, Dv$_{50}$ = 78.2 μm and Dv$_{90}$ = 112 μm, through laser size diffraction (ASTM B822), and impurities levels of 140 ppm C, 200 ppm Cu, 700 ppm N, 200 ppm O, 100 ppm P, 7500 ppm Si and 40 ppm S.

Additional powder feedstocks were also prepared with the addition of MoS$_2$ (Sigma-Aldrich) and MnS (Sigma-Aldrich) powder
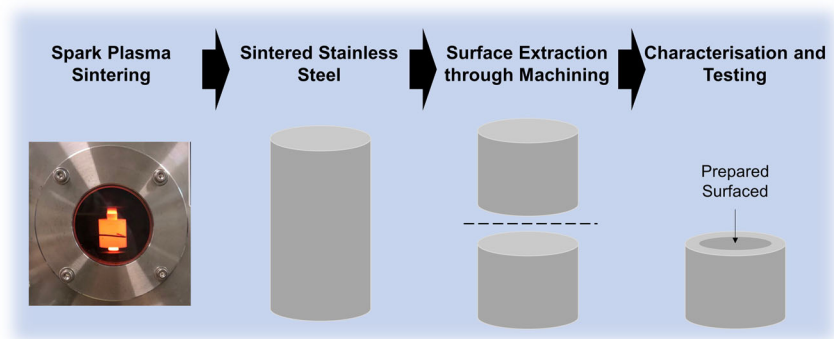
Fig. 13 Spark plasma sintering and sample preparation. Schematic showing the spark plasma sintering process, as well as the preparation of sample surface for characterisation and corrosion testing extracted from the mid-width of the sintered sample.

Table 3. Composition and nomenclature of 304L stainless steel powder feedstocks.	
Powder feedstock	**Content**
304L powder	As received 304L powder
304L-MnS	As received 304L powder + MnS (addition of 0.02 wt% S by mass)
304L-MoS$_2$	As received 304L powder + MoS$_2$ (addition of 0.02 wt% S by mass)
Powder feedstock preparation and their naming convention.	

(an additional 0.02 wt% of S added by mass) into the as received AISI 304L Stainless steel powder. The feedstocks were mixed through mechanical tumbling for 1 h. The prepared powder feedstocks and their naming conventions for the rest of this work are summarized in Table 3.

Spark plasma sintering
Sintering of the samples was carried out with a Dr. Sinter Lab Jr. Series 632Lx spark plasma sintering machine. Approximately 5 g of prepared powder feedstock was placed in the carbon mould of the spark sintering machine and then heated at a rate of 100 K per minute from room temperature to 1273 K. The temperature was controlled through a thermocouple attached to the carbon mould. Upon reaching 1273 K, the sample was held isothermally for 10 min. The entire sintering process was carried out in a low vacuum environment of <10 Pa, with a constant pressure of 30 MPa applied to the sample via a graphite punch. After the sintering process, the sample was left to cool to room temperature under a vacuum before it was removed from the sintering apparatus. The samples were subsequently extracted from the carbon mould.

Surface preparation
Carbon contamination is a well-known issue during the spark plasma sintering process[46,47], due to the high-temperature diffusion of carbon from the carbon mould and carbon papers that are used as spacers. To minimize the influence of the carbon contamination, especially from the surfaces in direct contact with the carbon parts during sintering, the sintered sample was sectioned at mid-width through wire cutting, as illustrated in the schematic of Fig. 13. The extracted surface was then ground and polished to either 0.05 μm for surface characterisation or 1200 grit for corrosion testing.

Characterisation methods
Scanning electron microscope (SEM) was performed with a Supra 40 SEM at an accelerating voltage of 20 keV. An Oxford Instruments EDX attachment allowed elemental compositions and mappings to be obtained. X-ray Diffraction (XRD) patterns were obtained with Bruker D8 Advance. A Cu(kα) source is deployed, with a primary beam path of 1600 W (40 kV and 40 mA). Scan signals were obtained with a 2θ scan interval of 0.02°, at a rate of 0.2 s per step. Optical Microscope images were taken with the aid of an Olympus GX51 inverted metallurgical microscope. X-ray Photoelectron Spectroscopy (XPS) was performed with a Kratos Analytical AMICUS XPS. A magnesium X-ray source was used, with the spectra collected at a step of 0.1 eV with a dwell time of at least 500 ms. Tougaard background subtraction was preferentially applied[48]. The positions and the identity of the Cr2p, Fe2p and O1s peaks were referenced from the work of Jung et al.[49].

Thermodynamic calculations
In addition to experimental investigations, thermodynamic calculations were performed to predict the interactions between the Fe-, Mn- and Mo-based sulfide inclusions using the reaction web module found on Fact-Web[50], deploying the FactPS - the FACT pure substances database (2022).

REFERENCES
1. Holmes, R. J., Lu, Y. & Lu, L. In *Iron Ore* 1–56 (Elsevier, 2022).
2. Deev, G. F., Popovich, V. V., Palash, V. N. & Karikh, V. V. Role of iron sulfide in the formation of cracks in weld joints. *Sov. Mater. Sci.* **18**, 288–290 (1982).
3. Gubenko, S. I. & Galkin, A. M. Nature of the red-shortness of steel. *Met. Sci. Heat. Treat.* **26**, 732–737 (1984).
4. Wranglén, G. Review article on the influence of sulphide inclusions on the corrodibility of Fe and steel. *Corros. Sci.* **9**, 585–602 (1969).
5. Schrama, F. N. H., Beunder, E. M., Van den Berg, B., Yang, Y. & Boom, R. Sulphur removal in ironmaking and oxygen steelmaking. *Ironmak. Steelmak.* **44**, 333–343 (2017).
6. Maciejewski, J. The effects of sulfide inclusions on mechanical properties and failures of steel components. *J. Fail. Anal. Prev.* **15**, 169–178 (2015).
7. Tanaka, Y., Pahlevani, F., Moon, S.-C., Dippenaar, R. & Sahajwalla, V. In situ characterisation of MnS precipitation in high carbon steel. *Sci. Rep.* **9**, 10096 (2019).

8. Lu, Y. & Miki, T. Thermodynamics of molten MnS–FeS and CrS–FeS system at 1843 K. *Isij. Int.* **61**, 2345–2354 (2021).

9. Rieders, N., Nandasiri, M., Mogk, D. & Avci, R. New insights into sulfide inclusions in 1018 carbon steels. *Metals* **11**, 428 (2021).

10. Liu, P., Zhang, Q. H., Watanabe, Y., Shoji, T. & Cao, F. H. A critical review of the recent advances in inclusion-triggered localized corrosion in steel. *NPJ Mater. Degrad.* **6**, 1–17 (2022).

11. Wranglen, G. Pitting and sulphide inclusions in steel. *Corros. Sci.* **14**, 331–349 (1974).

12. Newman, R. C. The dissolution and passivation kinetics of stainless alloys containing molybdenum—II. Dissolution kinetics in artificial pits. *Corros. Sci.* **25**, 341–350 (1985).

13. Kaneko, M. & Isaacs, H. S. Effects of molybdenum on the pitting of ferritic- and austenitic-stainless steels in bromide and chloride solutions. *Corros. Sci.* **44**, 1825–1834 (2002).

14. Polo, J. L., Cano, E. & Bastidas, J. M. An impedance study on the influence of molybdenum in stainless steel pitting corrosion. *J. Electroanal. Chem.* **537**, 183–187 (2002).

15. Pardo, A. et al. Effect of Mo and Mn additions on the corrosion behaviour of AISI 304 and 316 stainless steels in H2SO4. *Corros. Sci.* **50**, 780–794 (2008).

16. Lynch, B. et al. Passivation-induced Cr and Mo enrichments of 316L stainless steel surfaces and effects of controlled pre-oxidation. *J. Electrochem. Soc.* **167**, 141509 (2020).

17. Ha, H.-Y., Lee, T.-H., Bae, J.-H. & Chun, D. Molybdenum effects on pitting corrosion resistance of FeCrMnMoNC austenitic stainless steels. *Metals* **8**, 653 (2018).

18. Ali, M. et al. Electroslag refining of CrNiMoWMnV ultrahigh-strength steel. *J. Miner. Mater. Charact. Eng.* **05**, 385–407 (2017).

19. Clayton, C. R. & Lu, Y. C. A bipolar model of the passivity of stainless steel: the role of mo addition. *J. Electrochem. Soc.* **133**, 2465–2473 (1986).

20. Sugimoto, K. & Sawada, Y. The role of molybdenum additions to austenitic stainless steels in the inhibition of pitting in acid chloride solutions. *Corros. Sci.* **17**, 425–445 (1977).

21. Montemor, M. F., Simões, A. M. P., Ferreira, M. G. S. & Belo, M. D. C. The role of Mo in the chemical composition and semiconductive behaviour of oxide films formed on stainless steels. *Corros. Sci.* **41**, 17–34 (1999).

22. Blackwood, D. J. Can the point defect model explain the influence of temperature and anion size on pitting of stainless steels. *Corros. Sci. Tech.* **14**, 253–260 (2015).

23. Punckt, C. et al. Sudden onset of pitting corrosion on stainless steel as a critical phenomenon. *Science* **305**, 1133–1136 (2004).

24. Hashimoto, K., Naka, M., Asami, K. & Masumoto, T. An x-ray photo-electron spectroscopy study of the passivity of amorphous Fe-Mo alloys. *Corros. Sci.* **19**, 165–170 (1979).

25. Jin, H., Blackwood, D. J., Wang, Y., Ng, M.-F. & Tan, T. L. First-principles study of surface orientation dependent corrosion of BCC iron. *Corros. Sci.* **196**, 110029 (2022).

26. Ilevbare, G. O. & Burstein, G. T. The role of alloyed molybdenum in the inhibition of pitting corrosion in stainless steels. *Corros. Sci.* **43**, 485–513 (2001).

27. Kovalov, D., Taylor, C. D., Heinrich, H. & Kelly, R. G. Operando electrochemical TEM, ex-situ SEM and atomistic modeling studies of MnS dissolution and its role in triggering pitting corrosion in 304L stainless steel. *Corros. Sci.* **199**, 110184 (2022).

28. Kucernak, A. R. J., Peat, R. & Williams, D. E. Dissolution and reaction of sulfide inclusions in stainless steel imaged using scanning laser photoelectrochemical microscopy. *J. Electrochem. Soc.* **139**, 2337–2340 (1992).

29. Davoodi, A., Pakshir, M., Babaiee, M. & Ebrahimi, G. R. A comparative H2S corrosion study of 304L and 316L stainless steels in acidic media. *Corros. Sci.* **53**, 399–408 (2011).

30. Ng, M.-F., Blackwood, D. J., Jin, H. & Tan, T. L. Revisiting Cl-induced degradation of MnS inclusions using DFT. *J. Phys. Chem. C.* **125**, 24189–24195 (2021).

31. Sugimoto, K. & Sawada, Y. The role of alloyed molybdenum in austenitic stainless steels in the inhibition of pitting in neutral halide solutions. *Corrosion* **32**, 347–352 (1976).

32. Ryan, M. P., Williams, D. E., Chater, R. J., Hutton, B. M. & McPhail, D. S. Why stainless steel corrodes. *Nature* **415**, 770–774 (2002).

33. Nishimoto, M., Muto, I., Sugawara, Y. & Hara, N. Passivity of (Mn,Cr)S inclusions in type 304 stainless steel: the role of Cr and the critical concentration for preventing inclusion dissolution in NaCl solution. *Corros. Sci.* **176**, 109060 (2020).

34. Nishimoto, M., Muto, I., Sugawara, Y. & Hara, N. Morphological characteristics of trenching around MnS inclusions in type 316 stainless steel: the role of molybdenum in pitting corrosion resistance. *J. Electrochem. Soc.* **166**, C3081–C3089 (2019).

35. Wang, P. et al. Preparation of high-performance ultrafine-grained AISI 304L stainless steel under high temperature and pressure. *Prog. Nat. Sci.* **26**, 404–410 (2016).

36. Hillert, M. & Qiu, C. In *The SGTE Casebook* 106–113 (Elsevier, 2008).

37. Vicente, A. et al. The use of duplex stainless steel filler metals to avoid hot cracking in GTAW welding of austenitic stainless steel AISI 316L. *Int. J. Adv. Eng. Res. Sci.* **7**, 345–355 (2020).

38. Ke, R. & Alkire, R. Surface analysis of corrosion pits initiated at MnS inclusions in 304 stainless steel. *J. Electrochem. Soc.* **139**, 1573–1580 (1992).

39. Yang, S., Zhao, M., Feng, J., Li, J. & Liu, C. Induced-pitting behaviors of MnS inclusions in steel. *High. Temp. Mater. Proc.* **37**, 1007–1016 (2018).

40. Stewart, J. & Williams, D. E. The initiation of pitting corrosion on austenitic stainless steel: on the role and importance of sulphide inclusions. *Corros. Sci.* **33**, 457–474 (1992).

41. Chiba, A., Muto, I., Sugawara, Y. & Hara, N. Pit initiation mechanism at MnS inclusions in stainless steel: synergistic effect of elemental sulfur and chloride ions. *J. Electrochem. Soc.* **160**, C511–C520 (2013).

42. Chang, S. Y., Oh, S.-T., Suk, M.-J. & Hong, C. S. Spark plasma sintering of stainless steel powders fabricated by high energy ball milling. *J. Korean. Powd. Met. Inst.* **21**, 97–101 (2014).

43. Abdullah, Z., Ismail, A. & Ahmad, S. The influence of porosity on corrosion attack of austenitic stainless steel. *J. Phys. Conf. Ser.* **914**, 012013 (2017).

44. Yang, D. et al. Influence of porosity on mechanical and corrosion properties of SLM 316L stainless steel. *Appl. Phys. A* **128**, 51 (2022).

45. Zhang, H., Du, N., Wang, S., Zhao, Q. & Zhou, W. Determination of iron valence states around pits and the influence of Fe^{3+} on the pitting corrosion of 304 stainless steel. *Materials* **13**, 726 (2020).

46. Wang, P. et al. Influence of spark plasma sintering conditions on microstructure, carbon contamination, and transmittance of CaF2 ceramics. *J. Eur. Ceram. Soc.* **42**, 245–257 (2022).

47. Hříbalová, S. & Pabst, W. Theoretical study of the influence of carbon contamination on the transparency of spinel ceramics prepared by spark plasma sintering (SPS). *J. Eur. Ceram. Soc.* **41**, 4337–4342 (2021).

48. Repoux, M. Comparison of background removal methods for XPS. *Surf. Interface Anal.* **18**, 567–570 (1992).

49. Jung, R.-H., Tsuchiya, H. & Fujimoto, S. XPS characterization of passive films formed on Type 304 stainless steel in humid atmosphere. *Corros. Sci.* **58**, 62–68 (2012).

50. Bale, C. W. & Bélisle, E. Fact-Web suite of interactive programs www.factsage.com (2002).

AUTHOR CONTRIBUTIONS

D.J.B. conceived the study and directed the research project. K.X.K. performed the experiments. All authors analysed the data. K.X.K. drafted the manuscript. All authors reviewed and edited the manuscript.

COMPETING INTERESTS

The authors declare no competing interests.

ADDITIONAL INFORMATION

Correspondence and requests for materials should be addressed to Daniel J. Blackwood.

Reprints and permission information is available at http://www.nature.com/reprints

Publisher's note Springer Nature remains neutral with regard to jurisdictional claims in published maps and institutional affiliations.